ROYAL SOCIETY
OF CHEMISTRY

PAPER

Check for updates

Size-matching encapsulation of a high-nuclearity Ni-containing polyoxometalate into a light-responsive MOF for robust photogeneration of hydrogen†

Ruijie Wang, Yeqin Feng, Le Jiao, Yuanyuan Dong, Hui Zhou, Tianfu Liu, * Xuemeng Jing and Hongjin Lv *

The development of robust host–guest composite photocatalysts has been considered as an interesting research direction for efficient photo-driven hydrogen evolution. In this work, an interesting size-matching strategy was adopted to construct the $Ni_{16}As_4P_4$@NU-1000 composite by encapsulating a high-nuclearity Ni-containing polyoxometalate, $[\{Ni_4(OH)_3AsO_4\}_4(B\text{-}a\text{-}PW_9O_{34})_4]^{28-}$ ($Ni_{16}As_4P_4$), guest into a mesoporous Zr-based MOF (NU-1000) host. Under optimized conditions, the resulting $Ni_{16}As_4P_4$@NU-1000 composite photocatalyst shows outstanding long-term photo-driven hydrogen evolution activity, achieving a hydrogen evolution of 1120 mmol g^{-1} and a TON of 28 600 after 120-hour Xe-lamp irradiation. The photocatalytic activity remains essentially unchanged for at least four successive recycling tests. Mechanistic insights revealed that the excellent and robust photocatalytic activity of the $Ni_{16}As_4P_4$@NU-1000 composite could be attributed to the synergistic cooperation of good light-responsive ability of the NU-1000 host, reversible multi-electron-catalytic properties of the structurally intact $Ni_{16}As_4P_4$ cluster, and the suitable host–guest size-matching effect.

Introduction

Green hydrogen fuel has been considered as one of the most promising chemical energy carriers due to its high energy density, free of greenhouse gas and volatile organic compound (VOC) emission, etc. Solar-driven hydrogen production has been widely considered as a promising approach in transforming and storing intermittent solar energy into chemical bonds (H_2 gas).[1–4] Polyoxometalates (POMs), a class of structurally well-defined inorganic metal oxygen clusters, have been widely utilized in solar-driven water splitting for hydrogen generation, due to their structural diversity and tunability, multi-electron-transfer properties, reversible redox chemistry, good structural stability, and thermal stability.[5–8] However, the high solubility of POMs in reported homogeneous or pseudo-homogeneous systems leads to the difficulty of recyclability during the catalytic processes.[9] To address these issues, a number of efficient and robust POM-based composite materials have therefore been developed,[10–16] which integrated POM catalytic active units and the support materials (such as TiO_2,[17] zeolite,[18] silica,[19] activated carbon,[20] metal–organic frameworks (MOFs),[21–24]

MOE Key Laboratory of Cluster Science, School of Chemistry and Chemical Engineering, Beijing Institute of Technology, Beijing 102488, P. R. China. E-mail: hlv@bit.edu.cn; liutf@bit.edu.cn

† Electronic supplementary information (ESI) available. See DOI: https://doi.org/10.1039/d2ta09606d

macro/supramolecules,[25] etc.) to construct heterogeneous hybrids. Among these different types of support materials, MOFs, composed of metal nodes and multi-topology organic linkers,[26] have been regarded as very attractive supports to incorporate functional units/catalysts due to their good photosensitivity, rich porous properties, and tunable host–guest interaction.[21–23,27–31]

To date, there are a few representative reports on POM@-MOF composites used in photocatalytic hydrogen production systems.[32–38] For instance, Lin's group reported the one-pot synthesis of POM@MOF composites by integrating the photosensitizing $[Ru(bpy)_3]^{2+}$-derived dicarboxylate ligands, $Zr_6(\mu_3\text{-}O)_4(\mu_3\text{-}OH)_4$ secondary building units, and Wells–Dawson-type POMs. The resulting POM@MOF composites exhibited enhanced multielectron injection from the photoactive framework to the encapsulated redox-active POMs upon photoexcitation, leading to efficient visible-light-driven hydrogen production.[33] In addition, Zhang and co-workers constructed a series of Wells–Dawson-type POM@PSs@MOF composite materials (POMs = $P_2W_{15}V_3$, $P_2W_{17}Ni$, and $P_2W_{17}Co$; PS = $[Ru(bpy)_3]^{2+}$) via a charge-regulated sequential adsorption method, which exhibited higher heterogeneous photocatalytic activity than that of the corresponding homogeneous catalytic system.[35] To address the challenge of using noble metal photosensitive units ($[Ru(bpy)_3]^{2+}$, $[Ir(ppy)_2(bpy)]^+$) in these POM@MOF composites, we have recently reported two noble-

This journal is © The Royal Society of Chemistry 2023

J. Mater. Chem. A, 2023, 11, 5811–5818 | 5811

metal-free POM@MOF composites, Ni_3PW_{10}@NU-1000 and $Ni_3P_2W_{16}$@NU-1000, by incorporating a tri-Ni-substituted Keggin-type $K_6Na[Ni_3(H_2O)_3PW_{10}O_{39}H_2O]$ (Ni_3PW_{10}) and a Wells–Dawson-type $Na_4Li_5[Ni_3(OH)_3(H_2O)_3P_2W_{16}O_{59}]$ ($Ni_3P_2W_{16}$) POMs into a mesoporous photo-responsive Zr-based metal–organic framework (NU-1000).[37] Due to the better size match between the $Ni_3P_2W_{16}$ POM guest and MOF, the Ni_3P_2-W_{16}@NU-1000 composite exhibited superior long-term stability and reusability in the solar-driven water splitting reaction compared to that of the Ni_3PW_{10}@NU-1000 composite. In this context, it would be of great interest to explore the appropriate size match between the POM guest clusters and the pores of the NU-1000 MOF host for more robust light-driven hydrogen generation.

In this work, we have constructed a $Ni_{16}As_4P_4$@NU-1000 composite photocatalyst by integrating a high-nuclearity Ni-containing polyoxometalate, $[\{Ni_4(OH)_3AsO_4\}_4(B-a-PW_9O_{34})_4]^{28-}$ ($Ni_{16}As_4P_4$), into a mesoporous Zr-based MOF (NU-1000) *via* a well-established impregnation method. The molecular size of the $Ni_{16}As_4P_4$ (21.2 Å × 21.3 Å) guest cluster appropriately matches with the mesopores (31 Å × 31 Å) of the NU-1000 host. Under optimized conditions, the resulting Ni_{16}-As_4P_4@NU-1000 composite exhibited outstanding photocatalytic performance with a hydrogen evolution of 1120 mmol g^{-1} and turnover number (TON) of 28 600 under Xe lamp illumination. Recycling photocatalytic tests and long-term illumination experiments indicated that the $Ni_{16}As_4P_4$@NU-1000 composite showed superior long-term stability and reusability.

Results and discussion

The synthetic approaches for the $Ni_{16}As_4P_4$ POM cluster and NU-1000 MOF are described in detail in the Experimental section, and different $Ni_{16}As_4P_4$@NU-1000 composites were prepared using a well-established impregnation method.[37] Fig. 1 shows the scanning electron microscopy (SEM) and high-resolution transmission electron microscope (HR-TEM) images of NU-1000 only and the 0.1-$Ni_{16}As_4P_4$@NU-1000 composite. The similar SEM images (Fig. 1a and b) illustrated that the encapsulation of the POM guest cluster had no effect on the morphology of the NU-1000 host. The corresponding energy dispersive X-ray spectroscopy (EDS) mapping images suggested the existence and the uniform distribution of $Ni_{16}As_4P_4$ cluster in the NU-1000 host (Fig. 1). Compared to the HR-TEM image of NU-1000 (Fig. 1c), deep dark dots were clearly observed in the image of the 0.1-$Ni_{16}As_4P_4$@NU-1000 composite (Fig. 1d), further indicating the successful incorporation of $Ni_{16}As_4P_4$ clusters into the NU-1000 host. The powder X-ray diffraction (PXRD) patterns of $Ni_{16}As_4P_4$, NU-1000, and 0.1-$Ni_{16}As_4P_4$@NU-1000 are shown in Fig. S1.† It is noted that no characteristic diffraction peak of $Ni_{16}As_4P_4$ was observed in the PXRD pattern of 0.1-$Ni_{16}As_4P_4$@NU-1000, which could be attributed to the good dispersion of $Ni_{16}As_4P_4$ guest clusters in the pores of the NU-1000 host. In addition, the slight decrease in the PXRD diffraction intensity of the 0.1-$Ni_{16}As_4P_4$@NU-1000 composite indicated that the introduction of $Ni_{16}As_4P_4$ guest clusters still can partially affect the crystallinity of NU-1000 during the solution-based impregnation process. In addition, we have also further characterized the physical properties of NU-1000 and the 0.1-$Ni_{16}As_4P_4$@NU-1000 composite through Brunauer–Emmett–Teller (BET) measurement. The hysteresis loops observed in the low-temperature N_2 adsorption–desorption isotherms of NU-1000 only and the 0.1-$Ni_{16}As_4P_4$@NU-1000 composite (Fig. 2a) were basically associated with the typical microporous and mesoporous channels of the NU-1000 host (Fig. 2b). The calculated specific surface area of NU-1000 and 0.1-$Ni_{16}As_4P_4$@NU-1000 were 2063 and 873 $m^2 g^{-1}$, respectively. The significantly decreased specific surface area provided solid evidence that $Ni_{16}As_4P_4$ clusters have been successfully embedded into the NU-1000 host, which was further supported by the changes in the low-temperature N_2 adsorption–desorption isotherms and pore size distribution curves of NU-1000 and 0.1-$Ni_{16}As_4P_4$@NU-1000 (Fig. 2). According to the pore texture of NU-1000 and the molecular size of the $Ni_{16}As_4P_4$ cluster, it is
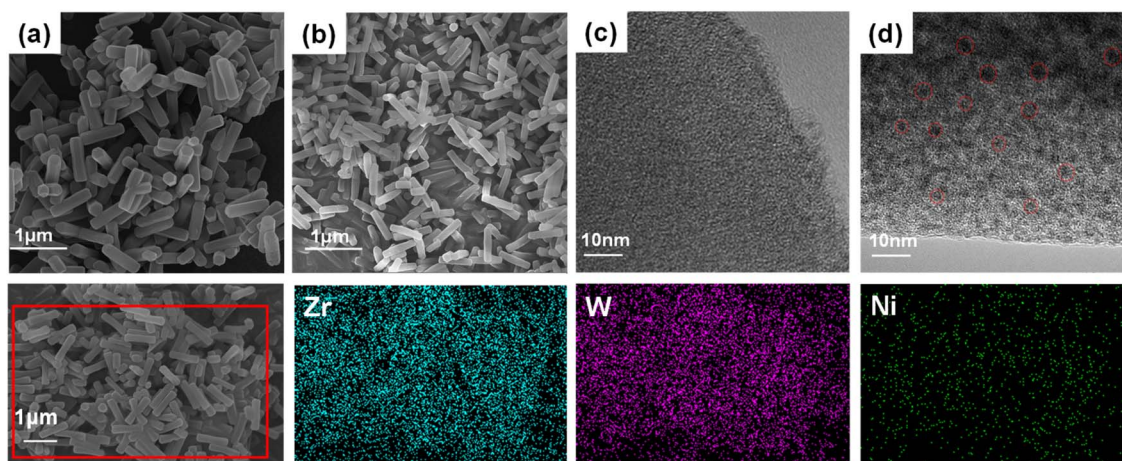

Fig. 1 SEM images of (a) NU-1000 only and the (b) 0.1-$Ni_{16}As_4P_4$@NU-1000 composite, and HR-TEM images of (c) NU-1000 only and the (d) 0.1-$Ni_{16}As_4P_4$@NU-1000 composite.

5812 | *J. Mater. Chem. A*, 2023, **11**, 5811–5818

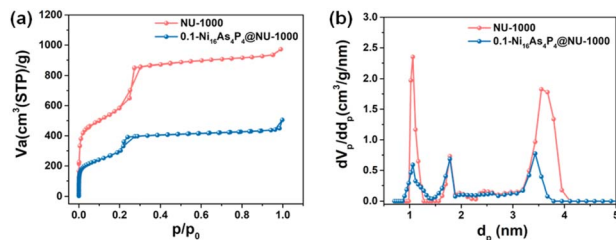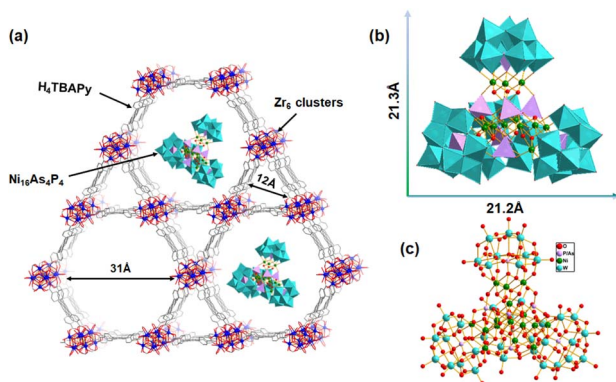This journal is © The Royal Society of Chemistry 2023

Fig. 2 (a) Low-temperature N_2 adsorption–desorption isotherms and (b) the pore size distribution curves of NU-1000 and 0.1-$Ni_{16}As_4$-P_4@NU-1000.

Fig. 3 (a) FT-IR spectra and (b) UV–Vis diffuse reflectance spectra of 0.1-$Ni_{16}As_4P_4$@NU-1000, NU-1000, and $Ni_{16}As_4P_4$.

Scheme 1 (a) Schematic representation of the possible structure for the $Ni_{16}As_4P_4$@NU-1000 composite. (b) Polyhedral and (c) ball-and-stick representations of the $Ni_{16}As_4P_4$ cluster.

speculated that the mesopores of the NU-1000 host should be mainly occupied by the $Ni_{16}As_4P_4$ cluster (Scheme 1). However, the intensity of micropores in the pore distribution curves (Fig. 2b) also decreased a bit, which might be caused by the incomplete removal of solvent molecules or the occupation of the $Ni_{16}As_4P_4$ cluster *via* a different orientation. It is also noted that the encapsulation of $Ni_{16}As_4P_4$ cluster does not completely block the mesopores of the NU-1000 host, which should be attributed to a relatively low loading quantity of POM clusters. In addition, linear EDS analysis was further carried out to prove the existence of POM clusters in the pores of the NU-1000 host (Fig S2†). The counts of Zr element exhibited rich and consistent abundance along the scanning direction shown in Fig S2b.† In contrast, the counts of W and Ni elements displayed a volcano shape (Fig S2c and d),† indicating that $Ni_{16}As_4P_4$ clusters were mainly incorporated into the specific channels of NU-1000 instead of simply on the surface of the NU-1000 host. And the lower counts of Ni and W elements were attributed to their relatively low loading quantity in the 0.1-$Ni_{16}As_4P_4$@NU-1000 sample.

The successful immobilization of the $Ni_{16}As_4P_4$ cluster as well as the physicochemical interactions were further investigated by the Fourier transform infrared (FT-IR) spectra measurements as shown in Fig. 3a. The characteristic IR signals from 700 to 1100 cm^{-1} were attributed to the typical W–O and P–O vibrational bands of the $Ni_{16}As_4P_4$ cluster, while the bands
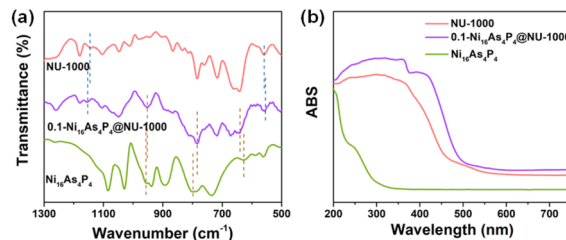
from 650 to 1200 cm^{-1} were assigned to the Zr–O vibrational modes and carboxylate stretches in NU-1000. Obviously, the FT-IR spectrum of 0.1-$Ni_{16}As_4P_4$@NU-1000 contained the characteristic IR vibration peaks of the $Ni_{16}As_4P_4$ guest cluster and NU-1000 host. Moreover, a slight shift of the vibrational peaks of the $Ni_{16}As_4P_4$ cluster was observed in the spectra of the 0.1-$Ni_{16}As_4P_4$@NU-1000 composite, which to some extent implied the electrostatic interaction between the $Ni_{16}As_4P_4$ cluster and NU-1000 host. Moreover, UV–Vis diffuse reflectance spectra (UV-DRS) were also utilized to characterize the optical absorption properties of these series of samples. The enhanced light absorption ability and the extended absorption edge of 0.1-$Ni_{16}As_4P_4$@NU-1000 further confirmed the electronic interaction between the host and guest (Fig. 3b).

The photocatalytic hydrogen evolution tests were carried out in a custom-built reactor equipped with a quartz window under external light illumination under constant magnetic stirring. The detailed procedures have been described in the Experimental section. To achieve optimal photocatalytic conditions, a series of parameters have been optimized regarding the preparation and photocatalytic systems of the $Ni_{16}As_4P_4$@NU-1000 composite, including the feedstock molar ratio of $Ni_{16}As_4P_4$ to NU-1000 in different composites, the pH of the reaction solution, the concentration of AA, and the usage amount of the photocatalyst. Specifically, the amount of hydrogen production increased with the increasing feedstock molar ratio of $Ni_{16}As_4P_4$ to NU-1000, reaching a peak value of 59 180 μmol g^{-1} with an apparent quantum yield (AQY) of 1.715% (see calculation details in the ESI†) at the feedstock molar ratio of 0.1 after 6-hour catalysis, and then decreased with the further increased feedstock molar ratio (Fig. 4a). Such volcanic trends of hydrogen production could be attributed to the changes in the pore textures of the $Ni_{16}As_4P_4$@NU-1000 composite. According to the results of BET measurement, both the BET surface area and the adsorption volume of 0.1-$Ni_{16}As_4P_4$@NU-1000 greatly declined compared to that of NU-1000 only (Fig. 2), revealing that the pores of the NU-1000 host would be mostly blocked on further increasing the feeding amount of $Ni_{16}As_4P_4$. The highly blocked pores in the composite would decrease the mass-transfer processes during photocatalysis, thereby resulting in a decrease in the photocatalytic hydrogen evolution activities. The photocatalytic activities of 0.1-$Ni_{16}As_4P_4$@NU-1000 also depended on the pH value of the reaction solution; the optimized pH value was obtained as pH = 5.5 because AA works as an efficient hole scavenger at this pH

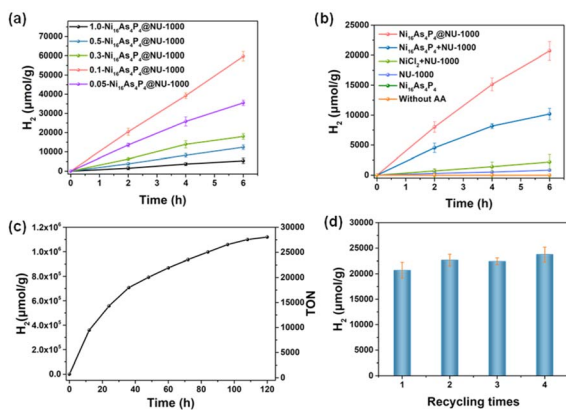This journal is © The Royal Society of Chemistry 2023

J. Mater. Chem. A, 2023, **11**, 5811–5818 | **5813**

Fig. 4 (a) The hydrogen production of x-$Ni_{16}As_4P_4$@NU-1000 photocatalysts with different feedstock molar ratios of $Ni_{16}As_4P_4$/NU-1000 (1.0–0.05). (b) Comparison profiles of the photocatalytic hydrogen production using different catalysts and reaction conditions. (c) Long-term photocatalytic hydrogen evolution test of 0.1-$Ni_{16}As_4P_4$@NU-1000. (d) Recycling photocatalytic tests for 0.1-$Ni_{16}As_4P_4$@NU-1000. Conditions: (a) 2 mg (b) 5 mg (c) 0.1 mg (d) 5 mg of photocatalyst, 20 mL of 1 M AA aqueous solution at pH = 5.5, Xe-lamp (full spectrum, 300 W, 20 °C).

(Fig. S3†). Meanwhile, the concentration of AA was optimized as 1 mol L^{-1} (Fig. S4†). In addition, the TON of the 0.1-$Ni_{16}As_4P_4$@NU-1000-catalyzing system reached 3080 at an optimized 0.1 mg photocatalyst usage (Fig. S5†), corresponding to a hydrogen evolution of 120 460 μmol g^{-1}. The higher photocatalyst usage resulted in a decrease in hydrogen production, which was probably caused by the strong light scattering effect, leading to a waste of incident photons.

Our previous studies revealed that the synergistic cooperation between the NU-1000 host and POM guest catalyst is beneficial to efficient photocatalytic hydrogen evolution.[37] Herein, control experiments in the absence of each component (NU-1000, $Ni_{16}As_4P_4$, and AA) yield no or negligible hydrogen production, indicating the importance of each component in the photocatalytic system for efficient catalysis (Fig. 4b). Further control experiments using $Ni_{16}As_4P_4$ + NU-1000 and $NiCl_2$ + NU-1000 as comparative catalysts have been also performed for photocatalytic hydrogen production under otherwise similar conditions (Fig. 4b). It is obvious that the 0.1-$Ni_{16}As_4P_4$@NU-1000 composite photocatalyst exhibited the best photocatalytic activity, indicating that the close integration of $Ni_{16}As_4P_4$ and NU-1000 as confirmed by FT-IR (Fig. 3a) and UV-Vis analyses (Fig. 3b) can facilitate the multiple photoelectron injection from the excited NU-1000 host to $Ni_{16}As_4P_4$ cluster for subsequent photocatalysis. Moreover, the catalytic systems of using either 0.1-$Ni_{16}As_4P_4$@NU-1000 or $Ni_{16}As_4P_4$ + NU-1000 both exhibited better performance than that of $NiCl_2$ + NU-1000, strongly implying that the unique structural integrity of nickel substitution in the $Ni_{16}As_4P_4$ cluster played a crucial role in effective photocatalytic hydrogen production. In addition, various spectroscopic analyses including FT-TR spectra (Fig. S6†), and SEM (Fig. S7†), and TEM images (Fig. S8†) also confirmed the structural intactness of the 0.1-$Ni_{16}As_4P_4$@NU-1000 composite after photocatalysis, demonstrating the good

photocatalytic stability and strong host–guest interaction in the composite.

To further evaluate the photocatalytic stability of the 0.1-$Ni_{16}As_4P_4$@NU-1000 composite, long-term photocatalytic hydrogen evolution was performed under the optimal photocatalytic conditions (Fig. 4c). With prolonged photocatalysis, the amount of hydrogen production gradually increased, achieving a hydrogen production of 1120 mmol g^{-1} and a TON of 28 600 after 120-hour illumination. Table S1† compared the photocatalytic activities of our present 0.1-$Ni_{16}As_4P_4$@NU-1000 composite with that of other reported POM@MOF composites for photocatalytic hydrogen evolution. It is clear that the 0.1-$Ni_{16}As_4P_4$@NU-1000 composite exhibited the best photocatalytic hydrogen evolution activity; the increased number of Ni centers may offer more active sites for catalysis.[37] Fig. 4d shows the recycling stability test results for the 0.1-$Ni_{16}As_4P_4$@NU-1000 composite. After four successive recycles, the hydrogen production remained largely unchanged, illustrating the good recycling stability of the 0.1-$Ni_{16}As_4P_4$@NU-1000 composite. The slight increase in hydrogen evolution activity after the first run could be ascribed to the improved utilization of absorbed photons due to better dispersion of the photocatalyst during photocatalysis. It is worth mentioning that the Keggin- or Dawson-type POM@NU-1000 composites exhibited decreased catalytic activity with recycling times as reported in our previous work, and the larger size of POM is beneficial for more robust catalysis.[37] Also, the long-term TON of the catalytic system using 0.1-$Ni_{16}As_4P_4$@NU-1000 was more than twice of the reported system using $Ni_3P_2W_{16}$@NU-1000, further implying that the appropriate size-matching strategy between the POM guest and the MOF host was beneficial for good photocatalytic performance. Based on the above experimental results and our previous observation,[37] it is concluded that the optimal size match between the $Ni_{16}As_4P_4$ guest clusters and the pores of the NU-1000 host could effectively prevent the leakage of the $Ni_{16}As_4P_4$ cluster during photocatalysis, thereby resulting in great recycling stability of the 0.1-$Ni_{16}As_4P_4$@NU-1000 composite.

In order to investigate the photocatalytic mechanism, the steady-state luminescence spectra of NU-1000 and the 0.1-$Ni_{16}As_4P_4$@NU-1000 composite were first collected using 365 nm laser light excitation (Fig. 5a). Upon excitation, an obviously strong photoluminescence signal was observed for
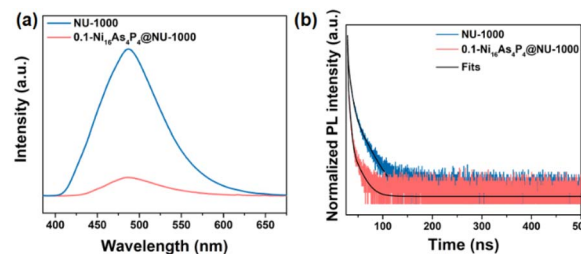

Fig. 5 (a) Luminescence spectra of 0.1-$Ni_{16}As_4P_4$@NU-1000 and NU-1000 with the excitation wavelength of 365 nm. (b) Normalized luminescence decay kinetics curves of NU-1000 and 0.1-$Ni_{16}As_4$-P_4@NU-1000.

5814 | J. Mater. Chem. A, 2023, 11, 5811–5818

This journal is © The Royal Society of Chemistry 2023

the pristine NU-1000 host, which can be dramatically quenched after incorporating $Ni_{16}As_4P_4$ clusters, indicating the efficient migration of photogenerated electrons from the excited NU-1000 framework to $Ni_{16}As_4P_4$ cluster in the $Ni_{16}As_4P_4$@NU-1000 composite. The photoluminescence decay kinetics analyses were further employed to study the photogenerated charge carrier dynamics in pristine NU-1000 and the 0.1-$Ni_{16}As_4P_4$@-NU-1000 composite (Fig. 5b). The decay curves were optimally fitted with a three-exponential decay function and the fitting results are summarized in Table S2.† Compared to the pristine NU-1000 host, the photoluminescence lifetimes of the 0.1-$Ni_{16}As_4P_4$@NU-1000 composite significantly decreased, which further revealed the effective transfer of photogenerated electrons between the NU-1000 host and $Ni_{16}As_4P_4$ guest.

In addition, the X-ray photoelectron spectroscopy (XPS) technique was further employed to determine the chemical oxidation states of Zr, W, and Ni elements in both the NU-1000 host and 0.1-$Ni_{16}As_4P_4$@NU-1000 composite (Fig. 6). The XPS signal of Zr can be deconvoluted into two peaks located at 184.4 eV (Zr $3d_{3/2}$) and 182.0 eV (Zr $3d_{5/2}$), respectively, revealing the existence of Zr^{4+} species in the NU-1000 framework (Fig. 6a). There was an obvious positive shift (~0.89 eV) observed for Zr 3d signal peaks after immobilization of $Ni_{16}As_4P_4$ into the NU-1000 framework, suggesting the shift of electron density around {Zr_6} nodes of NU-1000 to $Ni_{16}As_4P_4$ guest clusters due to strong electronic interactions. These results were consistent with the results of steady-state and time-resolved photoluminescence quenching behavior of NU-1000 after the incorporation of $Ni_{16}As_4P_4$ clusters. After photocatalysis, the Zr 3d signal peaks shifted back to a similar value to that of Zr 3d signal peaks in NU-1000 only, which should be attributed to the slight reduction of {Zr_6} nodes under the strong reducing environment. The XPS peaks of Ni were deconvoluted into Ni $2p_{1/2}$ and Ni $2p_{3/2}$ peaks with the corresponding binding energies of 874.4 eV and 856.5 eV in the $Ni_{16}As_4P_4$@NU-1000 composite, revealing the +2 oxidation state of the Ni centers in the POM clusters (Fig. 6b). The binding energies of W $4f_{5/2}$ and $4f_{7/2}$ were located at 38.0 eV and 35.9 eV corresponding to the +6 oxidation state of W (Fig. 6c). Both the Ni 2p and W 4f signal peaks shifted (~0.82 eV and ~0.17 eV) to the negative binding energy after photocatalysis, which indicated that

$Ni_{16}As_4P_4$ is partially reduced during the photocatalytic hydrogen evolution reaction.

Based on the above experimental observations and detailed analyses, the schematic energy level diagram to illustrate the photocatalytic hydrogen evolution mechanism was proposed as shown in Scheme 2. The HOMO–LUMO data of NU-1000 was obtained from a literature report,[39] while the LUMO position of $Ni_{16}As_4P_4$ was determined to be −0.220 V vs. NHE by the cyclic voltammetry (CV) test (Fig. S9†). During photocatalysis, the photo-responsive NU-1000 host can efficiently harvest photons and generate photoexcited states upon light irradiation, subsequently followed by the fast migration of photogenerated electrons to the $Ni_{16}As_4P_4$ guest clusters. To finish a complete catalytic cycle, the oxidation state of NU-1000 can be reduced back to the initial state using the sacrificial AA reagent; meanwhile, the reduced $Ni_{16}As_4P_4$ cluster catalyst will effectively reduce the adsorbed H^+ species to release hydrogen. Overall, the synergistic cooperation of the good light-responsive ability of the NU-1000 host, the reversible multi-electron-catalytic properties of the structurally intact $Ni_{16}As_4P_4$ cluster, and the suitable host–guest size-matching effect could greatly contribute to
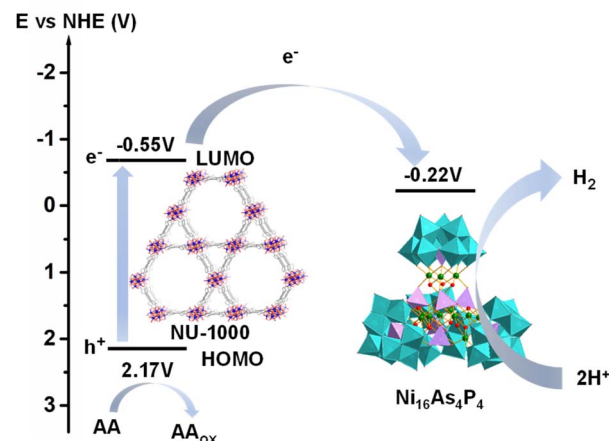
Scheme 2 Schematic energy level diagram of photocatalytic hydrogen production of the $Ni_{16}As_4P_4$@NU-1000 composite.

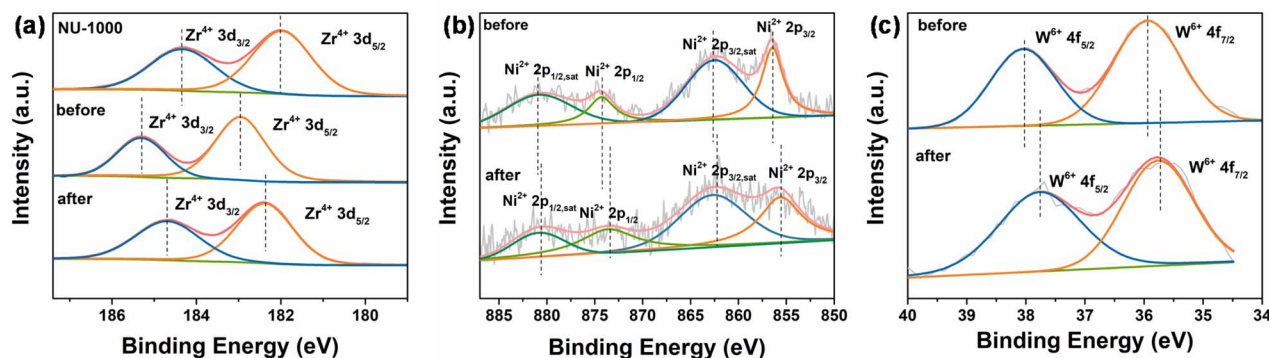**Fig. 6** High-resolution XPS spectra of (a) Zr 3d in NU-1000 and 0.1-$Ni_{16}As_4P_4$@NU-1000 before and after photocatalysis. The high-resolution XPS spectra of (b) Ni 2p and (c) W 4f of 0.1-$Ni_{16}As_4P_4$@NU-1000 before and after photocatalysis.

This journal is © The Royal Society of Chemistry 2023

J. Mater. Chem. A, 2023, **11**, 5811–5818 | **5815**

the superior photocatalytic activity of the **Ni$_{16}$As$_4$P$_4$**@NU-1000 composite.

Conclusions

In summary, we have successfully constructed a POM@MOF composite by immobilizing a high-nuclearity Ni-containing polyoxometalate, [{Ni$_4$(OH)$_3$AsO$_4$}$_4$(B-a-PW$_9$O$_{34}$)$_4$]$^{28-}$ (**Ni$_{16}$As$_4$P$_4$**), into a mesoporous Zr-based MOF (NU-1000) *via* a well-established impregnation approach. Various characterization techniques were employed to confirm the successful incorporation of **Ni$_{16}$As$_4$P$_4$** into the NU-1000 framework. Under optimized conditions, **Ni$_{16}$As$_4$P$_4$**@NU-1000 exhibited outstanding long-term photocatalytic activity with a hydrogen evolution of 1120 mmol g^{-1} and a TON of 28 600 during 120-hour Xe-lamp irradiation. Photophysical and spectroscopic analyses revealed that the excellent and robust photocatalytic activity of the **Ni$_{16}$As$_4$P$_4$**@NU-1000 composite can be attributed to the synergistic cooperation of good light-responsive ability of the NU-1000 host, reversible multi-electron-catalytic properties of the structurally intact **Ni$_{16}$As$_4$P$_4$** cluster, and the suitable host–guest size-matching effect. This work not only presented an interesting size-matching strategy for constructing a POM@MOF host–guest composite but also provided great potential in exploring more POM@MOF functional materials through host–guest interaction.

Experimental

Materials and methods

Chemicals were purchased from commercial sources and used without further purification. The scanning electron microscopy (SEM) images and energy dispersive X-ray spectroscopy (EDS) images were obtained on a ZEISS supra55. Fourier transform infrared (FT-IR) spectra were recorded on a Bruker Tensor II with KBr pellets. UV–Vis diffuse reflectance spectra (DRS) were recorded on a Techcomp UV 2600 spectrophotometer. Inductively coupled plasma emission spectroscopy (ICP-AES) data were obtained on a Spectro Arcos EOP (axial view inductively coupled plasma spectrometer). X-ray photoelectron spectroscopy (XPS) data were collected on a PHI 5000 VersaProbe III scanning XPS microprobe. Powder X-ray diffraction (PXRD) patterns were measured on a MiniFlex 600 diffractometer with a Cu Kα X-ray radiation source. The Brunauer–Emmett–Teller (BET) tests were performed on a Quantachrome Instruments ASiQMVH002-5 using a low-temperature N$_2$ adsorption–desorption method by pretreating the samples for 12 h under vacuum at 120 °C to obtain the clean surface. The fluorescence quenching spectra were collected on an Edinburgh FS50. Transmission electron microscope (TEM) images were obtained on a JEOL JEM-2100. Cyclic voltammetry (CV) curves were collected using a CHI660E electrochemical potentiostat with a three-electrode system comprising a glassy carbon working electrode, a Pt wire auxiliary electrode, and a saturated Ag/AgCl reference electrode. The amount of hydrogen production was determined using a Techcomp GC7900 gas chromatograph equipped with a thermal conductivity detector (TCD).

Synthetic procedures

Na$_{28}$[{Ni$_4$(OH)$_3$AsO$_4$}$_4$(B-a-PW$_9$O$_{34}$)$_4$]·120H$_2$O (Ni$_{16}$As$_4$P$_4$) preparation. The synthesis of **Ni$_{16}$As$_4$P$_4$** was conducted based on a previous method.[40] The typical synthetic procedure is described as follows. Na$_2$WO$_4$·2H$_2$O (16.5 g, 50 mmol) was first dissolved in 80 mL deionized water followed by adding Na$_2$-HAsO$_4$·7H$_2$O (1.72 g, 5.5 mmol) and adjusting the solution pH to 8.1 with concentrated acetic acid to obtain solution mixture A. 35 mL Ni(OOCCH$_3$)$_2$·4H$_2$O (4.1 g, 16 mmol) aqueous solution was then added into mixture A under stirring to obtain solution mixture B. After refluxing for 2 hours at 120 °C, Na$_2$HPO$_4$ (4 g, 33 mmol) was added into solution mixture B and kept refluxing for another 9 hours. Upon hot filtration, the resulting filtrate was the mother liquor for crystal growth. After two weeks, millimeter-long green needle-shaped crystals were collected.

Synthesis of 1,3,6,8-tetrakis (*p*-benzoic acid) pyrene (H$_4$TBAPy). A mixture of 1,3,6,8-tetrabromopyrene (0.500 g, 0.97 mmol), (4-(methoxycarbonyl)phenyl)boronic acid (1.04 g, 5.8 mmol), tetrakis (triphenylphosphine) palladium (0.03 g, 0.026 mmol), and potassium tribasic phosphate (1.100 g, 5.3 mmol) was transferred to a 50 mL three-necked flask and then degassed for 0.5 h under an argon atmosphere. After adding dry dioxane (20 mL), the whole reaction system was purged with argon for an additional 30 min. The mixture was then heated at 130 °C for 72 h in an oil bath under vigorous stirring, followed by cooling down to room temperature and evaporating to dryness. The crude product was washed with deionized water, extracted with chloroform (three times with 50 mL), and dried by adding an appropriate amount of magnesium sulfate. The residue was refluxed in tetrahydrofuran at 70 °C for 2 h and then cooled to room temperature and filtered. The faint yellow intermediate product 1,3,6,8-tetrakis (4-(methoxycarbonyl) phenyl) pyrene (TBAPy) was obtained by drying in a vacuum oven at 70 °C for 24 h.

0.58 g (0.78 mmol) of TBAPy and 100 mL of THF/water (ratio 1 : 1) solution containing 1.5 g (37.5 mmol) NaOH were added into a 250 mL round bottom flask, and then the mixture was refluxed at 100 °C overnight under stirring. The excess solvent THF was removed by rotary evaporation and the resulting solid residue was re-dissolved in water to form a clear yellow solution, which was stirred at room temperature for 2 h and adjusted the pH to 1 with concentrated HCl. Upon washing with water several times, the resulting solid was re-dissolved in boiled DMF and then cooled down to room temperature and recrystallized with dichloromethane. The final product was dried in a vacuum oven at 120 °C for 72 h.[37,41,42]

Preparation of Zr$_6$(μ$_3$-OH)$_8$(OH)$_8$(TBAPy)$_2$ (NU-1000). NU-1000 was synthesized according to the previous literature.[37,42] ZrOCl·8H$_2$O (96 mg mmol) and benzoic acid were first dissolved in 8 mL DMF and then was heated for 1 h at 100 °C. After cooling to room temperature, 2 mL DMF solution of H$_4$TBAPy preheated at 100 °C for 1 h and trifluoroacetic acid (40 μL) were added into the above mixture. The yellow suspension was sonicated for 20 min and heated at 120 °C for 24 h, and then cooled down to room temperature and washed twice with DMF. The activation of NU-1000 was also based on a previous report.[37]

5816 | *J. Mater. Chem. A*, 2023, **11**, 5811–5818

This journal is © The Royal Society of Chemistry 2023

The preparation of x-Ni$_{16}$As$_4$P$_4$@NU-1000. 0.00091 mmol Ni$_{16}$As$_4$P$_4$ (11.74 mg) was dissolved in 5 mL deionized water, followed by adding 0.00910 mmol NU-1000 (20 mg) and sonicating for 20 min. After vigorous stirring at room temperature for 72 h, the mixture was subjected to centrifugation, washed with water and acetone in sequence. The resulting solid powder was further soaked in acetone overnight and then centrifuged and dried in a vacuum oven at 120 °C for 72 hours, obtaining the target sample denoted as 0.1-Ni$_{16}$As$_4$P$_4$@NU-1000 with the Ni$_{16}$As$_4$P$_4$/NU-1000 feedstock molar ratio of 1.0. The preparations of x-Ni$_{16}$As$_4$P$_4$@NU-1000 (x = 0.05, 0.1, 0.3, and 0.5) are similar to that of 0.1-Ni$_{16}$As$_4$P$_4$@NU-1000 by adjusting the feeding amount of Ni$_{16}$As$_4$P$_4$.

Photocatalytic hydrogen evolution experiments

The photocatalytic hydrogen evolution test was carried out in a custom-built reactor equipped with a quartz window under external light illumination under constant magnetic stirring. The typical photocatalytic hydrogen evolution experiment is described in detail as follows. A certain amount of Ni$_{16}$As$_4$P$_4$@NU-1000 was uniformly dispersed into 20 mL ascorbic acid solution (AA, at different concentrations and pH values) under magnetic stirring and degassed with Ar/CH$_4$ (4/1) to remove air, where CH$_4$ was used as an internal standard. The reactor was irradiated using a 300 W Xe lamp (full spectrum, PCX50C, Beijing Perfectlight Technology Co., Ltd.) cutoff filter as a light source. The reaction temperature was maintained at 20 °C using a water-cooling system. During photocatalysis, the headspace gas (100 μL) was withdrawn from the glass reactor using a Hamilton air-tight syringe and then injected into a gas chromatograph (Techcomp GC7900) equipped with a TCD and a 5 Å molecular sieve capillary column with argon carrier gas. The amount of generated H$_2$ was calculated based on the calibration curve corrected using the CH$_4$ internal standard. The TON of H$_2$ was calculated according to the following equation as commonly used in similar systems:[37,43,44]

$$\text{TON} = \frac{n\left(\frac{1}{2}\text{H}_2\right)}{n(\text{POM})}$$

Author contributions

Ruijie Wang: methodology, data curation, formal analysis, investigation, writing – original draft preparation. Yeqin Feng, Le Jiao, Hui Zhou and Xuemeng Jing: software, visualization, validation. Yuanyuan Dong: formal analysis, validation. Tianfu Liu: funding acquisition, project administration. Hongjin Lv: funding acquisition, project administration, conceptualization, supervision, validation, writing – reviewing and editing.

Conflicts of interest

There are no conflicts of interest to declare.

Acknowledgements

References

1 J. Hong, X. Xia, Y. Wang and R. Xu, *J. Mater. Chem.*, 2012, **22**, 15006–15012.

2 B. Mahler, V. Hoepfner, K. Liao and G. A. Ozin, *J. Am. Chem. Soc.*, 2014, **136**, 14121–14127.

3 H. Zhang, P. Zhang, M. Qiu, J. Dong, Y. Zhang and X. W. D. Lou, *Adv. Mater.*, 2019, **31**, 1804883.

4 J. Zhang, Y. Wang, J. Jin, J. Zhang, Z. Lin, F. Huang and J. Yu, *ACS Appl. Mater. Interfaces*, 2013, **5**, 10317–10324.

5 H. Lv, Y. V. Geletii, C. Zhao, J. W. Vickers, G. Zhu, Z. Luo, J. Song, T. Lian, D. G. Musaev and C. L. Hill, *Chem. Soc. Rev.*, 2012, **41**, 7572–7589.

6 W. Guo, H. Lv, Z. Chen, K. P. Sullivan, S. M. Lauinger, Y. Chi, J. M. Sumliner, T. Lian and C. L. Hill, *J. Mater. Chem. A*, 2016, **4**, 5952–5957.

7 M. Zhang, H. Li, J. Zhang, H. Lv and G.-Y. Yang, *Chin. J. Catal.*, 2021, **42**, 855–871.

8 T. Cui, L. Qin, F. Fu, X. Xin, H. Li, X. Fang and H. Lv, *Inorg. Chem.*, 2021, **60**, 4124–4132.

9 J. J. Walsh, A. M. Bond, R. J. Forster and T. E. Keyes, *Coord. Chem. Rev.*, 2016, **306**, 217–234.

10 Y. Ren, C. Du, S. Feng, C. Wang, Z. Kong, B. Yue and H. He, *CrystEngComm*, 2011, **13**, 7143–7148.

11 X.-X. Lu, Y.-H. Luo, C. Lu, X. Chen and H. Zhang, *J. Solid State Chem.*, 2015, **232**, 123–130.

12 Y. Guo and C. Hu, *J. Mol. Catal. A: Chem.*, 2007, **262**, 136–148.

13 B. Chakraborty, G. Gan-Or, M. Raula, E. Gadot and I. A. Weinstock, *Nat. Commun.*, 2018, **9**, 4896.

14 H. Ma, B. Liu, B. Li, L. Zhang, Y. G. Li, H. Q. Tan, H. Y. Zang and G. Zhu, *J. Am. Chem. Soc.*, 2016, **138**, 5897–5903.

15 X. Gao, J. Wang, Q. Xue, Y.-Y. Ma and Y. Gao, *ACS Appl. Nano Mater.*, 2021, **4**, 2126–2135.

16 P. Wang, L. Jiang, X. Zou, H. Tan, P. Zhang, J. Li, B. Liu and G. Zhu, *ACS Appl. Mater. Interfaces*, 2020, **12**, 25910–25919.

17 Y. Yang, Q. Wu, Y. Guo, C. Hu and E. Wang, *J. Mol. Catal. A: Chem.*, 2005, **225**, 203–212.

18 S. Pourbeyram, M. Moosavifar and V. Hasanzadeh, *J. Electroanal. Chem.*, 2014, **714–715**, 19–24.

19 Y. Yang, Y. Guo, C. Hu, Y. Wang and E. Wang, *Appl. Catal., A*, 2004, **273**, 201–210.

20 F. M. Toma, A. Sartorel, M. Iurlo, M. Carraro, P. Parisse, C. Maccato, S. Rapino, B. R. Gonzalez, H. Amenitsch, T. Da Ros, L. Casalis, A. Goldoni, M. Marcaccio, G. Scorrano, G. Scoles, F. Paolucci, M. Prato and M. Bonchio, *Nat. Chem.*, 2010, **2**, 826–831.

This journal is © The Royal Society of Chemistry 2023

J. Mater. Chem. A, 2023, **11**, 5811–5818 | **5817**

21 C. M. Granadeiro, P. Silva, V. K. Saini, F. A. A. Paz, J. Pires, L. Cunha-Silva and S. S. Balula, *Catal. Today*, 2013, **218–219**, 35–42.

22 N. Maksimchuk, M. Timofeeva, M. Melgunov, A. Shmakov, Y. Chesalov, D. Dybtsev, V. Fedin and O. Kholdeeva, *J. Catal.*, 2008, **257**, 315–323.

23 J. W. Sun, P. F. Yan, G. H. An, J. Q. Sha, G. M. Li and G. Y. Yang, *Sci. Rep.*, 2016, **6**, 25595.

24 Y. Benseghir, A. Lemarchand, M. Duguet, P. Mialane, M. Gomez-Mingot, C. Roch-Marchal, T. Pino, M. H. Ha-Thi, M. Haouas, M. Fontecave, A. Dolbecq, C. Sassoye and C. Mellot-Draznieks, *J. Am. Chem. Soc.*, 2020, **142**, 9428–9438.

25 L. X. Cai, S. C. Li, D. N. Yan, L. P. Zhou, F. Guo and Q. F. Sun, *J. Am. Chem. Soc.*, 2018, **140**, 4869–4876.

26 A. Dhakshinamoorthy, A. M. Asiri and H. Garcia, *Angew. Chem., Int. Ed.*, 2016, **55**, 5414–5445.

27 G. Paille, M. Gomez-Mingot, C. Roch-Marchal, B. Lassalle-Kaiser, P. Mialane, M. Fontecave, C. Mellot-Draznieks and A. Dolbecq, *J. Am. Chem. Soc.*, 2018, **140**, 3613–3618.

28 W. Salomon, F. J. Yazigi, C. Roch-Marchal, P. Mialane, P. Horcajada, C. Serre, M. Haouas, F. Taulelle and A. Dolbecq, *Dalton Trans.*, 2014, **43**, 12698–12705.

29 E. V. Ramos-Fernandez, C. Pieters, B. van der Linden, J. Juan-Alcañiz, P. Serra-Crespo, M. W. G. M. Verhoeven, H. Niemantsverdriet, J. Gascon and F. Kapteijn, *J. Catal.*, 2012, **289**, 42–52.

30 S.-X. L. Chun-Yan Sun, D.-D. Liang, K.-Z. Shao, Y.-H. Ren and Z.-M. Su, *J. Am. Chem. Soc.*, 2009, **131**, 1883–1888.

31 L. Zeng, X. Guo, C. He and C. Duan, *ACS Catal.*, 2016, **6**, 7935–7947.

32 J. Han, D. Wang, Y. Du, S. Xi, Z. Chen, S. Yin, T. Zhou and R. Xu, *Appl. Catal., A*, 2016, **521**, 83–89.

33 Z. M. Zhang, T. Zhang, C. Wang, Z. Lin, L. S. Long and W. Lin, *J. Am. Chem. Soc.*, 2015, **137**, 3197–3200.

34 X. J. Kong, Z. Lin, Z. M. Zhang, T. Zhang and W. Lin, *Angew. Chem., Int. Ed.*, 2016, **55**, 6411–6416.

35 H. Li, S. Yao, H.-L. Wu, J.-Y. Qu, Z.-M. Zhang, T.-B. Lu, W. Lin and E.-B. Wang, *Appl. Catal., B*, 2018, **224**, 46–52.

36 D. Shi, R. Zheng, C. S. Liu, D. M. Chen, J. Zhao and M. Du, *Inorg. Chem.*, 2019, **58**, 7229–7235.

37 L. Jiao, Y. Dong, X. Xin, L. Qin and H. Lv, *Appl. Catal., B*, 2021, **291**, 120091.

38 L. Jiao, Y. Dong, X. Xin, R. Wang and H. Lv, *J. Mater. Chem. A*, 2021, **9**, 19725–19733.

39 P. P. Bag, X.-S. Wang, P. Sahoo, J. Xiong and R. Cao, *Catal. Sci. Technol.*, 2017, **7**, 5113–5119.

40 H. Lv, Y. Chi, J. van Leusen, P. Kögerler, Z. Chen, J. Bacsa, Y. V. Geletii, W. Guo, T. Lian and C. L. Hill, *Chem.–Eur. J.*, 2015, **21**, 17363–17370.

41 J. E. Mondloch, W. Bury, D. Fairen-Jimenez, S. Kwon, E. J. DeMarco, M. H. Weston, A. A. Sarjeant, S. T. Nguyen, P. C. Stair, R. Q. Snurr, O. K. Farha and J. T. Hupp, *J. Am. Chem. Soc.*, 2013, **135**, 10294–10297.

42 T. C. Wang, N. A. Vermeulen, I. S. Kim, A. B. F. Martinson, J. F. Stoddart, J. T. Hupp and O. K. Farha, *Nat. Protoc.*, 2015, **11**, 149–162.

43 X. J. Kong, Z. Lin, Z. M. Zhang, T. Zhang and W. Lin, *Angew. Chem., Int. Ed.*, 2016, **55**, 6411–6416.

44 J. Tian, Z. Y. Xu, D. W. Zhang, H. Wang, S. H. Xie, D. W. Xu, Y. H. Ren, H. Wang, Y. Liu and Z. T. Li, *Nat. Commun.*, 2016, **7**, 11580.

5818 | *J. Mater. Chem. A*, 2023, **11**, 5811–5818

This journal is © The Royal Society of Chemistry 2023